NUMERICAL INVESTIGATION OF HYBRID THERMAL MANAGEMENT SYSTEMS COMBINING PHASE CHANGE MATERIAL AND LIQUID COOLING FOR BATTERY MODULES IN REGIONAL ELECTRIC AIRCRAFT DURING NOMINAL OPERATION AND THERMAL RUNAWAY

E. K. Güngör*, A. O. Altun*, F. Franke*, S. Kazula*

* German Aerospace Center (DLR), Institute of Electrified Aero Engines, Lieberoser Straße 13a, Cottbus, Germany

Abstract

Lithium-Ion batteries serve as a promising energy carrier to achieve climate-neutral aviation. However, the battery thermal management system contributes significantly to the total module mass, which reduces the total specific energy of the battery system.

Hence, four hybrid thermal management concepts for a battery module are investigated, aiming to balance thermal performance with gravimetric power density. The investigated module consists of cylindrical Lithium-Ion batteries (LIB) and employs phase change material (PCM) for passive cooling as well as active liquid cooling.

The scope of the investigation encompasses two different active cooling systems: a cooling plate design, featuring a bottom cooling plate with intercellular PCM, and a thermal conductive structure (TCS) design incorporating a bottom-side PCM layer and intercellular TCS. For each design, a robustness-focused and a mass-minimizing version is investigated. While all designs effectively maintain optimal thermal homogeneity during standard missions, the TCS-based design shows superior thermal reserves at the cost of increased mass and manufacturing complexity, while the cooling-plate-based design demonstrated superior thermal homogeneity. The study quantifies the trade-off between gravimetric efficiency and thermal performance, identifying the mass-optimized version of the cooling plate design as the optimal trade-off for further investigation in a defined worst-case-scenario. Under this extreme thermal runaway scenario, the system is designed to prevent propagation to adjacent modules during a mandated ignition profile of 20 % of cells within 60 seconds, which is successfully demonstrated by the verified numerical results. Thus, this work provides a decision-making framework for designing inherently safe, lightweight energy storage in electric aviation.

Keywords

Electric aviation; Battery thermal management; Hybrid cooling; Phase change material; CFD

NOMENCLATURE

BTMS	Battery Thermal Management System
CFD	Computational Fluid Dynamics
CMT	Certification Management Team
DLR	Deutsches Zentrum für Luft- und Raumfahrt e.V.
LIB	Lithium-Ion-Battery
NMC	Nickel-Manganese-Cobalt
PCM	Phase Change Material
SAT	Sodium Acetate Trihydrate
TCS	Thermal Conductive Structure
THR	Total Heat Release
TR	Thermal Runaway
UDF	User Defined Function

1. INTRODUCTION

The aviation industry is undergoing a profound paradigm shift towards climate-neutral mobility. In alignment with the European Green Deal and Flightpath 2050 objectives [1], the electrification of propulsion systems for regional aircraft has emerged as a key technology. Lithium-ion batteries (LIBs) are a promising energy carrier in these architectures. However, the significant disparity in specific energy density between current LIB technology (250 $Wh\,kg^{-1}$ to 300 $Wh\,kg^{-1}$) and conventional jet fuel (12 000 $Wh\,kg^{-1}$) remains a fundamental obstacle [2], and the mass penalty of the battery thermal management system (BTMS) directly constrains payload and range [3].

Effective thermal management is essential for safe operation. LIBs require an optimal operating temperature window between 15 °C to 35 °C to prevent accelerated degradation and to mitigate the risk of thermal runaway (TR) [4]. TR is a self-accelerating chemical process that releases substantial heat and flammable gases, potentially triggering a system-wide cascade of hazardous effects such as uncontrollable fire [2, 5].

Current battery thermal management technologies primarily include air cooling, liquid cooling, passive cooling with phase change materials (PCM), and hybrid systems. While air-cooled systems are mechanically simple, they often fail to meet the high heat transfer requirements of high-density packs [4]. Furthermore, liquid cooling utilizing water-glycol mixtures possess the advantage of a superior heat transfer coefficient which is optimal for commercial electric vehicles [4]. However, standard liquid-cooled designs often neglect the compactness and weight-to-performance ratio critical for aviation [6]. Therefore, a design trade-off becomes necessary: thermal conductive structures (TCS) can enhance performance while requiring careful balancing against potential impacts on temperature homogeneity [7]. Passive PCM cooling offer excellent isothermal heat absorption during peak loads, but the low thermal conductivity remains a limiting factor [8]. Altun et al. [9] and Zhang et al. [10] propose hybrid configurations, combining PCM with active liquid cooling, to overcome the temporal limitations of purely passive systems.

Despite these advancements, the state of the art reveals a critical gap regarding the specific requirements of electric aviation. Most existing hybrid studies either focus on nominal operation optimization [11] or generic TR mitigation with small-scale modules [10]. Approaches such as immersion cooling often require mass-intensive setups incompatible with lightweight aircraft structures [12]. Consequently, further research is required to:

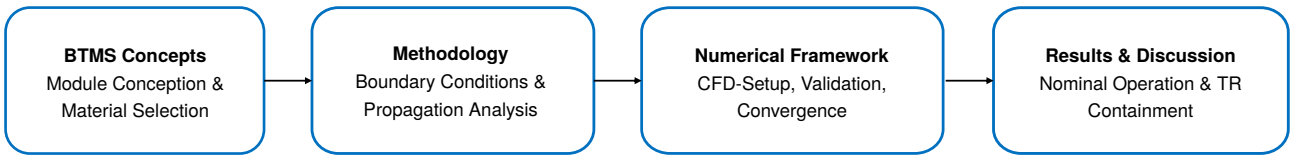


FIG 1. Methodological workflow and structural overview of the study, mapping the sequential progression from initial BTMS design and boundary definitions to numerical implementation and final performance evaluation.

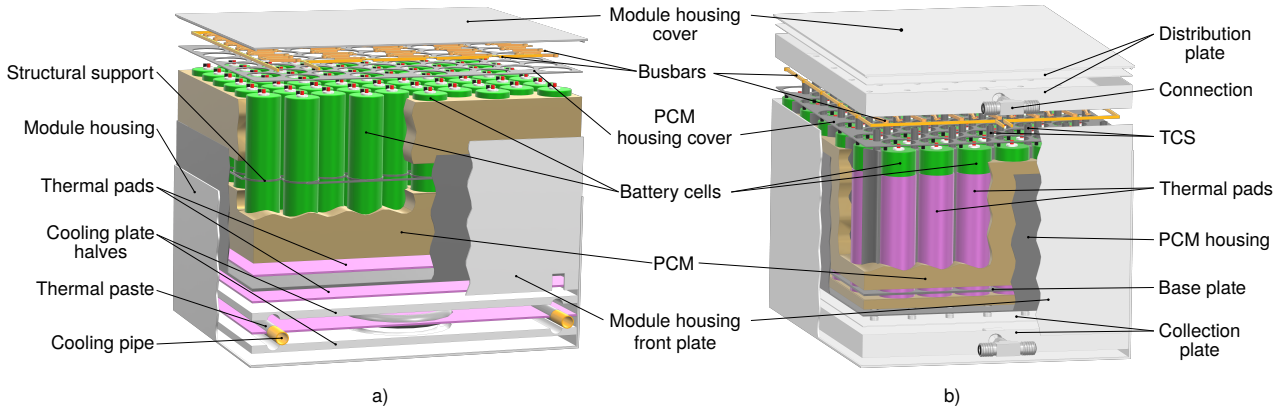


FIG 2. Exploded view of hybrid BTMS Design: a) CP-design: bottom cooling plate with intercellular PCM, b) TCS-design: intercellular TCS and bottom PCM.

1) Develop a compact module design aiming for aeronautical applications while considering efficient nominal operation and TR containment according to certification standards of major civil aviation authorities [13].
2) Evaluate these systems under transient mission profiles.
3) Resolve the inherent design conflict between high thermal conductivity for cooling and thermal isolation for mitigation of TR propagation to adjacent battery modules.

This paper addresses these gaps by evaluating four hybrid BTMS variants for a battery module featuring 65 18650 NMC cells. To achieve this, the study follows a structured methodology, which comprises the systematic design phase, physical and analytical modeling, high-fidelity transient CFD simulations, and a comprehensive evaluation. This process is illustrated in Fig. 1. The core objective is to determine whether these designs satisfy the stringent safety requirements mandated by major civil aviation authorities (EASA, FAA, TCCA ANAC), particularly regarding the prevention of TR propagation. Using a high-fidelity, transient CFD framework in Ansys Fluent, both a mission profile during nominal operation and a TR scenario are analysed. The findings show the potential of hybrid BTMS to serve as guidance for future studies for the design of inherently safe, lightweight battery storage systems for sustainable regional aviation.

2. DESIGN OF BTMS CONCEPTS

This study evaluates four hybrid BTMS variants, based on two different designs. The design implementation was carried out using the CAD software Siemens NX 2412.

2.1. Module conception

2.1.1. Cooling plate design: bottom cooling plate & intercellular PCM

The cooling plate (CP) design, shown in Fig. 2a, combines passive cooling via a PCM matrix embedding the cells with active cooling via a cooling plate at the base. The cooling plate consists of two aluminum halves with an embedded copper tube through which the coolant flows. Silicone-based thermal pads and thermal paste are used to improve heat conduction.
The cooling plate design is investigated in two variants: a robustness-focused version (CP-robust) as well as a mass-reduced version (CP-light). The geometric parameters of these variants are specified in Tab. 1.

2.1.2. TCS design: intercellular thermal conductive structures & bottom PCM layer

Based on the concept introduced by Lai et al. [6], a TCS-based design is developed. Shown in Fig. 2b, this design combines passive cooling via a PCM layer below the battery cells and active cooling via intercellular TCS. The TCS partially enclose the lateral surface areas, as can be seen in Fig. 4.

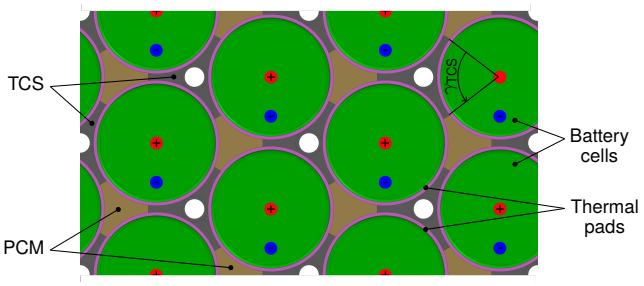
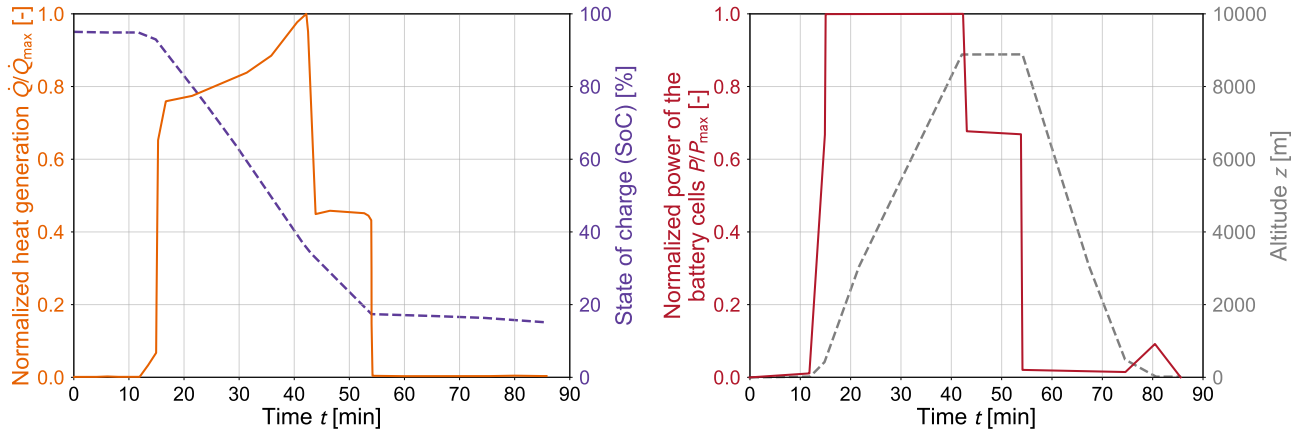


FIG 4. Top view of the internal layout of Design 2, illustrating the contact surface angle of the TCS, γ_{TCS}.



(a) Normalized heat flow $\dot{Q}/\dot{Q}_{max}$ and corresponding SOC of the battery cells over the flight duration.

(b) Altitude z and normalized electric power P/P_{max}.

FIG 3. Investigated thermal profile corresponding to the flight profile of a fully electric regional passenger flight for 250 passengers with a range of 649 km originating from the DLR project EXACT2.

The TCS, the PCM housing, and the base plate are manufactured from Ti-6Al-4V to ensure mechanical integrity and structural stability under the extreme thermal loads characteristic of TR events. To optimize the thermal contact between the cells and the TCS, thermal pads are inserted at the interfaces. The coolant is distributed to the 65 TCS via vertical outlets. After flowing through the TCS, the coolant is directed into a collection plate below the PCM layer.
Identically to the CP-based design, the TCS-based design is investigated in two variants: a robust version (TCS-robust) as well as a mass-reduced version (TCS-light). The geometric parameters of these variants are specified in Tab. 1.

TAB 1. Parameters and masses of BTMS versions.

Design	Parameter	Robust	Light
CP-based	PCM thickness [mm]	4.0	2.0
	Plate thickness [mm]	14.0	8.0
	Pipe inner diameter [mm]	8.0	6.0
	Pipe thickness [mm]	1.0	0.5
	Dry module mass [kg]	**6.59**	**5.04**
TCS-based	TCS contact surface angle γ_{TCS} [°]	75	45
	Dry module mass [kg]	**5.06**	**4.96**

2.2. Material selection

A mixture of water and ethylene glycol is selected as the coolant, offering a favorable balance between frost protection and high cooling performance as well as being industrially established, even though it has a higher viscosity than water and is toxic [11]. To satisfy the DLR design constraint of a maximum freezing temperature of the coolant of −20 °C, a mass fraction of ethylene glycol of 36 % is determined. It is assumed that the powertrain's waste heat is utilized to maintain the coolant temperature above the specified limit. An increase of the ethylene glycol content would further reduce the freezing point but simultaneously result in reduced cooling capacity and increased coolant mass and viscosity, thereby escalating the required pumping power and system mass.

For the passive thermal buffering, Sodium-acetate trihydrate (SAT) is identified as the optimal PCM based on the following criteria:

1) **Inherent non-flammability:** This is a critical requirement to prevent TR propagation via ignition of adjacent components, which renders organic PCMs unsuitable for this application. Due to its status as a hydrated salt, SAT is inherently non-flammable [14].
2) **Optimal phase change temperature:** SAT exhibits a phase change temperature of 58 °C [14], which exceeds the upper temperature threshold of 55 °C defined for transient peak loads. Furthermore, compared to high-temperature PCMs, SAT ensures rapid activation prior to the onset of a full-scale TR.
3) **Superior total heat capacity:** By combining a high thermal stability limit of 380 °C and a specific heat capacity of approximately 3.0 kJ kg^{-1} K^{-1} [14], SAT achieves a higher cumulative specific enthalpy change compared to other investigated inorganic PCMs with a phase change temperature in the same range, such as PCM Products's S-range or X-range. Additionally, the latent heat of fusion of Δh_m = 264 kJ kg^{-1} enables the absorption of substantial thermal energy during the initial TR phase.

3. METHODOLOGY

3.1. Boundary conditions

3.1.1. Thermal behavior under nominal operation

Thermal management requires precise knowledge of the internal heat sources. In this BTMS design study, the nominal operation and TR cases were investigated. The considered mission profile is based on the concept of a fully electric regional aircraft for 250 passengers with a range of 649 km that originates from the DLR project EXACT2. The resulting relationship between the state of charge (SOC) and the normalized heat rate $\dot{Q}/\dot{Q}_{max}$, shown in Fig. 3a, serves as the thermal boundary condition in the simulations under nominal operation. In Fig. 3b, the altitude and power profiles of the mission are depicted, allowing for the distinction of individual flight phases.

3.1.2. Thermal behavior under TR

To comply with aviation certification standards, effective TR containment is mandatory. Following the EASA regulations [13], the BTMS must prevent a propagation of TR to adjacent modules during simultaneous TR of 20 % of the battery cells within 60 seconds.
To evaluate this, a semi-empirical numerical model was developed based on experimental data for 18650 NMC cells. The model computes the total heat release (THR, measured in $\mathrm{kJ\,kg^{-1}}$) as a function of the SOC, applying a scaling factor to represent the higher energy density of next-generation cells. Specifically, the specific THR is formulated using piecewise cubic polynomials to capture the non-linear thermokinetics of NMC cells:

$$\mathrm{THR}(\mathrm{SOC}) = a_i(\mathrm{SOC} - \mathrm{SOC}_0)^3 + b_i(\mathrm{SOC} - \mathrm{SOC}_0)^2 + c_i(\mathrm{SOC} - \mathrm{SOC}_0) + d_i \tag{1}$$

where the coefficients a_i, b_i, c_i, d_i and reference shifts SOC_0 (corresponding to the lower bound of each interval) are defined piecewise across distinct SOC intervals to ensure a smooth shape-preserving transition. The resulting polynomial coefficients for each interval are detailed in Tab. 2. The transient heat release rate is determined by integrating experimental profiles that capture the distinct SOC-dependent thermokinetics. Within the CFD environment, a developed user defined function (UDF) dynamically triggers the heat source term based on the local cell temperature and current SOC, interpolating the appropriate transient heat release characteristics.

TAB 2. Piecewise cubic polynomial coefficients for the scaled specific THR across SOC intervals (units: a_i in $\mathrm{kJ\,kg^{-1}\,\%^{-3}}$, b_i in $\mathrm{kJ\,kg^{-1}\,\%^{-2}}$, c_i in $\mathrm{kJ\,kg^{-1}\,\%^{-1}}$, d_i in $\mathrm{kJ\,kg^{-1}}$).

SOC Interval	$a_i \times 10^{-6}$	$b_i \times 10^{-4}$	$c_i \times 10^{-2}$	d_i
100–73.6 %	−2.69	−3.82	2.51	1.49
73.6–25 %	−0.56	−3.00	2.90	0.78
25–0 %	−8.00	3.00	1.93	0.25

The data basis for THR relies on a meta-analysis of experimental data for 18650 NMC cells by Rappsilber et al. [15], utilizing precise measurements from copper sealed battery calorimeters to exclude external gas combustion effects. To account for next-generation high-energy cells ($\sim 450\,\mathrm{W\,h\,kg^{-1}}$) [16], a linear scaling factor of $f = 2.33$ is applied based on the specific energy correlation by Feng et al. [17]. The non-linear thermokinetics over the SOC are modeled using a shape-preserving piecewise cubic Hermite interpolating polynomial (PCHIP). The resulting discrete anchor points for the specific THR and ignition temperatures T_{ign} are summarized in Tab. 3.

TAB 3. Anchor points for SOC-dependent THR and ignition temperature.

SOC [%]	100	50	25	0
Scaled THR [kJ/kg]	1.84	1.31	0.78	0.25
T_{ign} [°C]	140	166	166	192

For prismatic battery modules, Belt and Sorensen [18] identified initiation of TR in the corner of the module as the most critical scenario due to the reduced effective contact area of edge-positioned cells for heat dissipation. Accordingly, the "corner case" in the rear left corner was selected in this work. The initiation sequence within the module is illustrated in Fig. 5. TR is initiated in the trigger cell and spreads to the immediately adjacent cells in the first propagation wave. Subsequently, TR propagates to the cells of the second wave. Accordingly, a total of 13 battery cells will have undergone TR which corresponds to 20 % of the battery cells inside the module, fulfilling the EASA requirement [13].

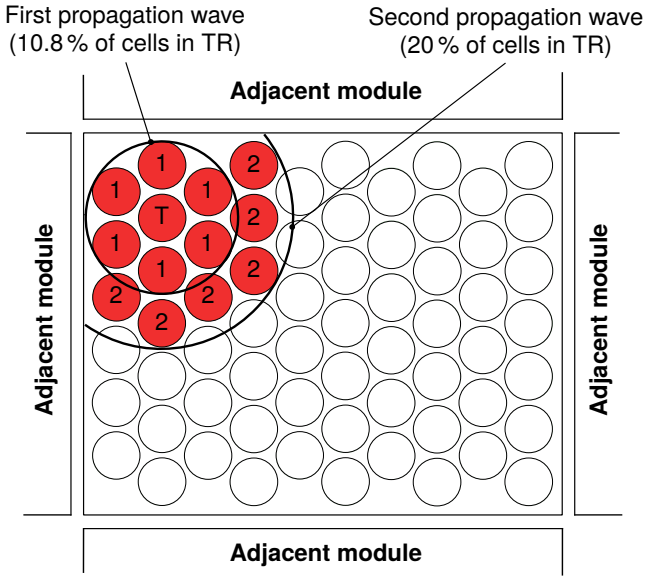


FIG 5. TR propagation scenario: The initiated cell is labeled "T". The first intra-module propagation wave encompasses the immediately adjacent cells, marked "1". Cells labeled "2" follow in the second intra-module propagation wave.

To mitigate the extreme thermal load during a TR event, the coolant mass flow rate of the active cooling system is increased. However, to prevent excessive parasitic power consumption by the coolant pump, a hydraulic constraint imposing a maximum allowable pressure drop of 25 kPa (0.25 bar) is established for the transient TR operating condition.

3.2. Analytical propagation analysis

To investigate thermal cascading to adjacent modules without requiring computationally intensive three dimensional modeling of the entire battery pack, a coupled transient one-dimensional multilayer post-processing model is employed. For this purpose, the layered structure between the modules is modeled locally as a finite, planar composite wall. This structure sequentially comprises the primary-side housing walls, the air gap, and the housing walls and PCM layer of the passive adjacent module, terminating with the first row of battery cells of the adjacent module. The spatial distribution of the numerically modeled and analytically extended parts of the geometry is shown in Fig. 6.
Transient heat conduction within this heterogeneous material stack is described by the one-dimensional heat conduction equation:

$$\rho(x)c_{\mathrm{p}}(x)\frac{\partial T}{\partial t} = \frac{\partial}{\partial x}\left(\lambda(x)\frac{\partial T}{\partial x}\right) \tag{2}$$

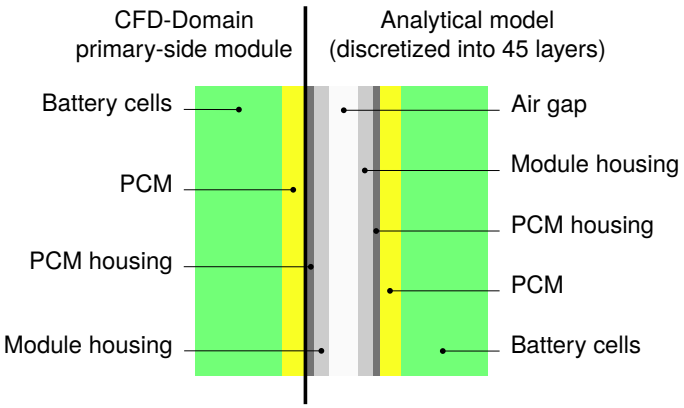


FIG 6. Boundary of numerically investigated geometry and analytical extension for propagation analysis.

where x denotes the spatial coordinate spanning from the primary-side housing wall toward the adjacent module, while $\rho(x)$, $c_p(x)$, and $\lambda(x)$ represent the local material density, specific heat capacity at constant pressure, and thermal conductivity, respectively.

For the numerical solution, the entire system is spatially discretized. The housing layers are resolved using $n = 5$ nodes each, whereas the thermally thick row of battery cells is discretized more finely with $n_{\mathrm{LIB}} = 20$ nodes, resulting in a total of $N_{\mathrm{total}} = 50$ nodes. The spatial step size Δx_m is defined specifically for each material layer m. Discretization is performed using the explicit finite difference method (forward time centered space scheme) utilizing central differences for the spatial domain and a forward difference quotient for the time domain. For an internal node k at discrete time step i (step size Δt), the update for the temperature T is given by:

$$T_{i+1,k} = T_{i,k} + \frac{\Delta t}{\rho_k c_{\mathrm{p},k} \Delta x_k} \left[\lambda_{k+\frac{1}{2}} \frac{T_{i,k+1} - T_{i,k}}{\Delta x_k} - \lambda_{k-\frac{1}{2}} \frac{T_{i,k} - T_{i,k-1}}{\Delta x_k} \right] \tag{3}$$

At the material interfaces ($k \pm \frac{1}{2}$), the abrupt change in thermal conductivity is represented by the harmonic mean of the adjacent layers.

A time-dependent Dirichlet boundary condition is imposed at the inlet node ($k = 0$), derived directly from the transient CFD simulation data of the primary-side PCM rear wall. The final node in the cell core ($k = N_{\mathrm{total}} - 1$) is defined as adiabatic, which conservatively represents the physical heat accumulation at the center of the cylindrical cell:

$$T_{i+1,N_{\mathrm{total}}-1} = T_{i,N_{\mathrm{total}}-1} + \frac{2\Delta t \lambda_{N_{\mathrm{total}}-1}}{\rho_{N_{\mathrm{total}}-1} c_{\mathrm{p},N_{\mathrm{total}}-1} \Delta x^2_{N_{\mathrm{total}}-1}} \left(T_{i,N_{\mathrm{total}}-2} - T_{i,N_{\mathrm{total}}-1} \right) \tag{4}$$

The time step Δt is dynamically adjusted so that the local grid Fourier number within each layer remains below the critical explicit stability limit ($\mathrm{Fo}_{\Delta x} = a\Delta t/\Delta x^2 \leq 0.50$).

Within the 5 mm-wide air gap, purely conductive heat transfer is initially assumed as an approximation. Since free convection is often suppressed in narrow gaps due to high confinement effects, this idealization ($\mathrm{Nu} \approx 1$, meaning that heat transfer is governed entirely by conduction while convective contributions remain negligible) is continuously verified during post-processing using the transient Rayleigh number. Propagation across modules is considered initiated if the calculated cell temperature at any node of the row of battery cells exceeds the critical, SOC-dependent ignition temperature as defined in sec. 3.1.2.

3.3. Aeronautical Constraints

Compared to the automotive sector, electric aviation is characterized by significantly higher sensitivity to mass, as the battery mass is a fixed system ballast and accordingly limits mission range and payload capacity [5]. Among other design goals and target values, the nominal operating temperature range, the maximum temperature difference within the module, and the coolant pressure drop are summarized are summarized in Tab. 4 and serve as an evaluation benchmark for the CFD results.

TAB 4. Quantitative design goals and thresholds for the hybrid BTMS.

Parameter	Requirement	Source / Rationale
T_{nom}	15 °C – 35 °C	State of health [19]
ΔT_{mod}	2 K – 3 K	Prevent uneven aging [19]
TR containment	at 20 % cells in TR	EASA requirement [13]
T_{freeze}	max. −20 °C	DLR constraint
Δp_{nom}	minimize	Reduce parasitic power
Δp_{TR}	$\leq$ 0.25 bar	DLR constraint
Mass efficiency	maximize	Maximize payload

3.4. Numerical Framework

3.4.1. CFD-Setup and solver configuration

Preprocessing was performed in Ansys Discovery and Design Modeler. The final polyhedral mesh was generated using the Watertight Geometry workflow in Ansys Fluent Meshing.

To enhance numerical efficiency, the geometries were selectively simplified during preprocessing. Components irrelevant to flow and heat transfer such as housings, busbars, and distribution/collection plates were removed. For the TCS-based design, the advantage of the symmetrical arrangement of the battery module was exploited and a symmetry plane was utilized to reduce the computational domain by 50 %, thereby significantly reducing computational effort while applying mirrored boundary conditions. Furthermore, the effects of cell venting during TR and the subsequent convectional heating of adjacent components was neglected.

During nominal operation simulations, the characteristic Reynolds number is well below the critical threshold for the laminar-to-turbulent transition ($\mathrm{Re} \approx 100 - 150$). Consequently, laminar modeling is physically justified. In TR simulations, the k-ω-SST-Modell is used to capture local instabilities. The PISO algorithm is selected for pressure-velocity coupling.

The numerical implementation of the developed TR model is carried out via a UDF written in C that calculates the source terms for each volume element as a function of the SOC. The TR source term is introduced using a ramp function (a linear increase over 1 s) to ensure the numerical stability of the pressure-velocity coupling in Fluent. TR is initiated in the first battery cell (Cell 58) by targeted heating

at the cell's geometric center to a temperature exceeding the ignition point, thereby triggering the UDF.

3.4.2. Validation

The experiment of Hassan et al. [20] is reproduced numerically to validate the coupling of heat conduction and convection. The iterative, spatial and temporal convergence were verified. Fig. 7 shows the comparison of the simulation results with the experimental data over a flow time of 691 s. While the deviation between the simulation and the experimental data from Hassan et al. [20] is below 0.5 % at the start, it rises to just under 8 % by the end of the simulated discharge period; however, since the calculated GCI_{fine} ($\approx$ 25 %) significantly exceeds the observed difference, the agreement with the experiment is interpreted as a fortuitous cancellation of discretization and modeling errors rather than as proof of complete grid independence. Nonetheless, the capture of the coupling of heat conduction and convection by the CFD software is considered as validated.

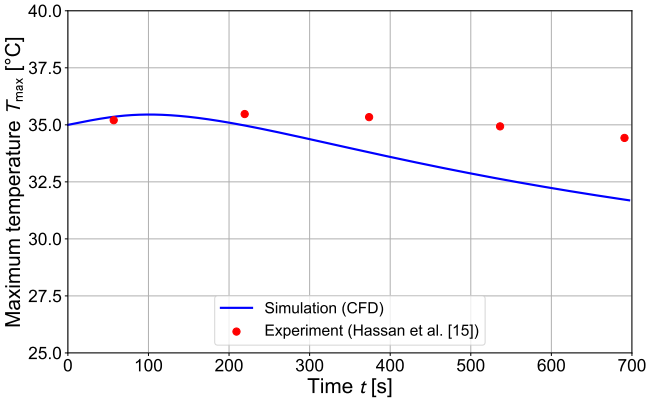


FIG 7. Validation of the CFD setup by replicating the experiment by Hassan et al. [20] and comparing the simulation results with the experimental data. The deviation between the simulation and the experimental data from Hassan et al. [20] rises to just under 8 % towards the end of the simulated time period.

In order to verify the quality of the developed semi-empirical TR-model, a validation against experimental data from Golubkov et al. [21] was performed. The grid and time-step independence were confirmed through systematic convergence studies. Subsequently, the numerical results were compared with experimental data. Fig. 8 shows the comparison of the battery cell surface temperature between simulation and experiment. While the deviation between the experimental and numerical results amounts to 11.3 % at the start, it decreases to 6.7 % at the end of the simulated time span. The active TR process and thus the main exothermic reaction phase concludes within approximately 60 s to 70 s. Beyond this period, the subsequent cooling phase observed in the experiments by Golubkov et al. [21] is governed primarily by ambient convection rather than internal reaction kinetics and is therefore outside the scope of the active TR model. With an average deviation of 8.09 %, the model is considered to accurately capture the kinetics of the main reaction phase.

3.4.3. Spatial convergence of BTMS-Designs

Discretization was performed using unstructured polyhedral grid. For the thin layers, discretization with at least

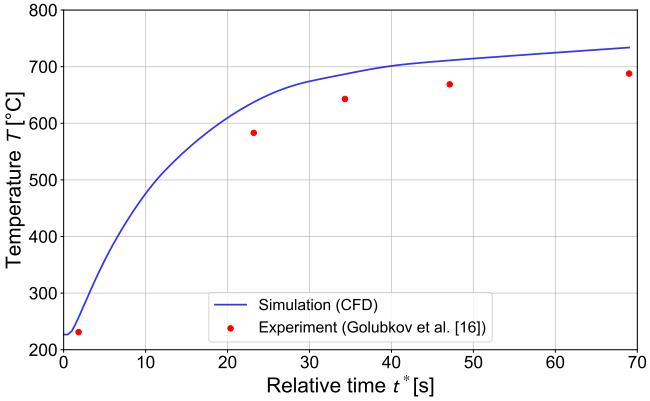


FIG 8. Validation of the TR model through comparison with experimental data. The time-dependent surface temperature profile of the battery cell shows an average deviation of less than 10 % between the experimental data from Golubkov et al. [21] and the simulation results.

three elements in the normal direction was ensured. A grid study as well as a time step study was performed. Due to the active cooling system being consistent through the robust and light versions of each design, convergence studies were performed for the robust version of each design and the results were transferred to the light versions. The grid convergence index GCI_{fine} amounted to 1.01 % for the grid study of the robust version of the CP-based design and 0.47 % for the robust version of the TCS-based design. The number of elements in the converged meshes are represented in Tab. 5.

TAB 5. Grid size of converged meshes.

Design	Version	Mesh Size
CP-based	robust	6,996,200
	light	5,526,739
TCS-based	robust	4,459,886
	light	5,061,175

4. RESULTS & DISCUSSION

4.1. Results under nominal operation

4.1.1. Comparative assessment of the designs

The spatial temperature distribution of the cells provides an initial qualitative overview of the cooling concepts investigated. Fig. 9 illustrates the surface temperatures at the end of the load phase (t = 52 min) using a uniform scale. This comparative display visually highlights the advantage of TCS cooling: while the CP-based cooling concepts (a, b) exhibit temperatures in the 28 °C range over large areas, the entire cell matrix of the TCS variants (c, d) remains significantly cooler.

For a detailed quantitative analysis of the four investigated BTMS, Fig. 10 shows the module-wide peak temperature, module-wide average temperature, maximum temperature difference between battery cells, and mass-flow-averaged coolant outlet temperature. Since the exothermic heat release of the battery cells during nominal operation only begins at t_{init} = 11.95 min (see

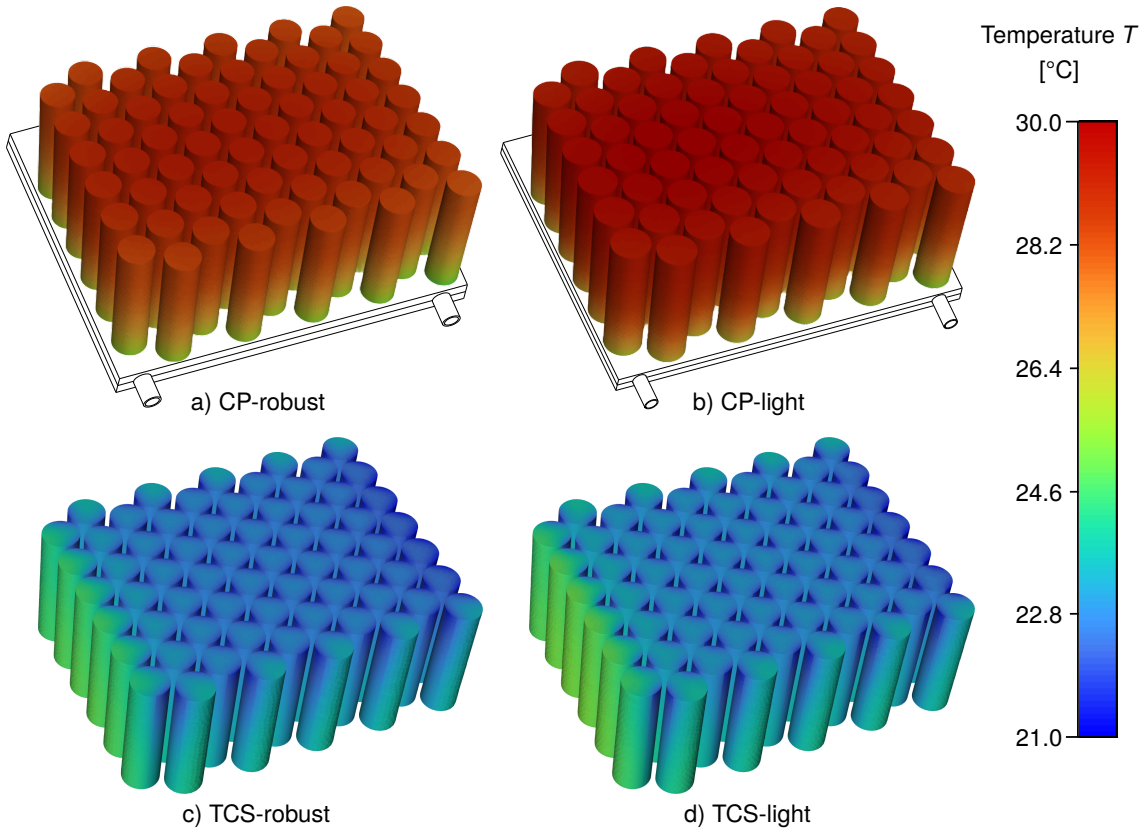


FIG 9. Surface temperatures of the battery cells at the end of the transient load profile (Nominal operation, $t \approx 54$ min). a) CP-robust, b) CP-light, c) TCS-robust, d) TCS-light.

Fig. 3a), the thermal behavior prior to this point is not presented here. Consequently, a relative time axis $t^* = t - t_{\text{init}}$ is introduced for the subsequent analysis, with the zero point ($t^* = 0$ s) corresponding to the exact moment heat release begins.

As can be seen in Figs. 10a and 10b, all BTMS meet the requirement of maintaining cell temperatures within 15 °C to 35 °C throughout the entire mission. However, the significantly higher thermal reserve of the TCS-based design is striking. While the peak temperature of CP-light exceeds the 30 °C mark at the time of peak load ($t^* \approx 30$ min), the temperature level of the TCS-based design stabilizes at approximately 25 °C.

An opposite trend is observed regarding the homogeneity of the temperature distribution (see Fig. 10c). Both versions of the TCS-based design exhibit temperature differences of up to 1.94 K and 2.25 K respectively, which is significantly superior to the versions of the CP-based design ($\approx$ 1.3 K to 1.4 K). These large temperature differences occur between the battery cells at the rear of the module, which border neighboring cells on only one side but are surrounded by TCS on both sides, and the cells at the front of the module, which are cooled by the TCS on one side only.

The higher temperature of the coolant at the TCS outlets shown in Fig. 10d consistently correlates with the more efficient heat removal through the TCS. While the coolant at the outlet of the cooling pipe in both CP-based versions exhibits less heating despite higher cell temperatures, the higher temperature level at the TCS outlets highlights the improved thermal contact and the associated higher total heat flux.

TAB 6. Thermal characteristics at the time of peak load ($t^* \approx$ 30 min).

Parameter	CP-based		TCS-based	
	robust	light	robust	light
T_{max} [°C]	29.17	30.06	25.47	25.66
T_{avg} [°C]	27.88	28.72	24.38	24.48
ΔT_{modul} [K]	1.31	1.29	1.94	2.25
h^*A [W K^{-1}]	12.72	11.72	37.87	39.00

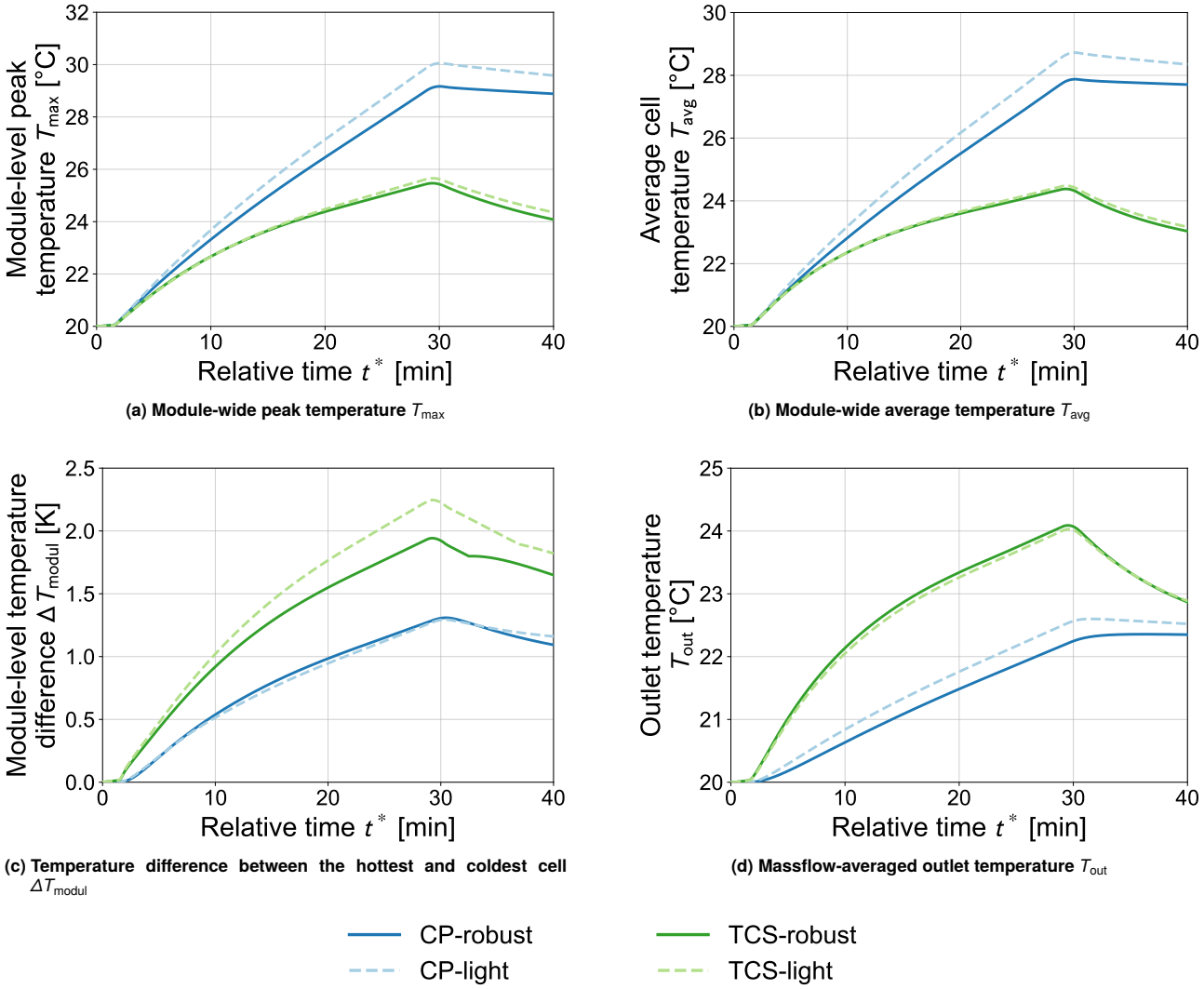
* Quasi-steady-state heat transfer coefficient h after completion of the thermal start-up phase.

Furthermore, Fig. 10a shows that reducing the TCS opening angle γ_{TCS} from 75° in the robust version to 45° in the mass-reduced version does not adversely affect the module-wide peak temperature or the average temperature of the battery cells. This indicates that this weight optimization does not result in a significant loss of cooling performance.

Tab. 6 summarizes the characteristic parameters at the time of peak load.

Furthermore, it is evident that the peak temperatures under the investigated load profile lie significantly below the lower limit of the phase change temperature of 50°C defined for the PCM selection. Consequently, alternative PCMs with higher heat capacities and lower phase change temperatures such as inflammable composite materials should be considered in future studies.

Although the TCS-based design offers the lowest battery cell temperatures, the CP-based design fully meets the requirements. Even at peak load, the peak temperatures remain well below the critical limit of 35 °C, at approxi-



(a) Module-wide peak temperature T_{max}

(b) Module-wide average temperature T_{avg}

(c) Temperature difference between the hottest and coldest cell ΔT_{modul}

(d) Massflow-averaged outlet temperature T_{out}

FIG 10. Thermal profiles of all cooling concepts over the relevant duration of the entire mission profile (t^* = 0 min to 40 min).

mately 30 °C. An additional sensitivity study conducted with a mass flow rate reduced to 13 % resulted in a temperature rise of only 2 K. This underscores that, despite its smaller wetted surface area, the CP-based design possesses sufficient margins for the mission profile. Furthermore, this design exhibits the best thermal homogeneity with a maximum temperature difference between cells of 1.29 K. According to Saw et al. [22], this is a crucial factor in effectively preventing uneven electrochemical cell aging.

The calculated peak temperatures under the selected load profile remaining significantly below the 35 °C limit is largely attributable to the conservative choice of a reference ambient temperature of T_{init} = 20 °C. This assumption reflects a moderate climate scenario and represents a lower bound regarding thermal stress.

Validation under extended ambient conditions is essential for the operation of a regional passenger aircraft intended to cover diverse mission scenarios such as hotter ambient conditions in Southern Europe. An increase in ambient temperature will reduce the cooling capacity of the active cooling system, leading to an overall rise in temperature levels given a constant rate of heat generation. To avoid performance losses and accelerated cell aging under such environmental conditions, pre-cooling the battery packs to a defined starting temperature prior to flight seems to be an effective operational strategy. In addition, future studies should evaluate the BTMS under higher discharge rates. According to Warner [19], higher discharge currents lead to a disproportionate increase in ohmic heat losses within the battery cells, significantly intensifying thermal dynamics and local heat generation within the module. While the PCM's buffer capacity and the thermal reserve of the active cooling systems examined provide a solid foundation, these factors must be quantified against increased load and environmental demands in an expanded sensitivity analysis to ensure the overall system's robustness across the entire operating range.

4.1.2. Discussion of mass efficiency and system complexity

The comparison of the investigated concepts regarding lightweight potential and mass efficiency in nominal operation is summarized in Tab. 7.

The increase in pressure drop from CP-robust to CP-light (by a factor of approximately 3) highlights the sensitivity of the pressure drop to the reduction in cross-section from 8 mm to 6 mm. Although the mass of the cooling plate was reduced, this advantage comes at the cost of a significantly higher power requirement for the pumping system. The advantages of CP-light is primarily evident in its structural simplicity and mass efficiency:

TAB 7. Comparison of mechanical and fluid-dynamic characteristics.

Parameter	CP-based		TCS-based	
	robust	light	robust	light
Coolant mass [g]	37.4	19.3	631	631
Battery cell mass fraction on module [%]	46.2	60.6	53.8	54.8
Δp^*_{tot} [Pa]	40.9	119.9	108.6	108.6

* Ref. value at the start of the simulation at T = 20 °C; decreases slightly due to viscosity changes.

- **Mass fraction:** With a mass fraction of the battery cells of 60.56 % in the filled state, CP-light is the lightest concept. Since the CP-based design requires only a minimal amount of coolant (19 g) compared to the TCS-based design (631 g), this advantage is almost entirely maintained in the filled state.
- **Manufacturing effort:** With 265 individual components, the complexity of the TCS-based design is almost twice that of the CP-based design (139 components). Accordingly, the conventional design of CP-light not only reduces the number of potential PCM leakage points at the interfaces between the TCS and the PCM housing as well as coolant leakage points at the connections to the distribution and collection plates, but also significantly minimizes the requirements regarding manufacturing tolerances and assembly processes.
- **Pressure loss:** Although the absolute pressure loss of 119.92 Pa is the highest compared to the other designs, it results in a hydraulic pumping power in the negligible milliwatt range; consequently, it does not compromise the aircraft's overall energy efficiency.

Overall, it was concluded that CP-light, the mass-reduced version of the CP-based design, represents the optimal compromise for the mission profile under consideration and thus to be further investigated in the TR scenario.

4.2. Analysis of the TR and containment

4.2.1. Implementation of TR initiation

The initiation of the first battery cell occurs at the moment when the exothermic heat release of the battery cells begins (t = 11.95 min). Although the trigger cell immediately released high-energy source terms, the analysis shows that the first propagation wave experiences hardly any temperature rise within the first 30 seconds, which is attributable to the thermal damping provided by the PCM. This indicates that the hybrid BTMS prevents intra-module propagation by overheating within a 30-second timeframe. To ensure EASA compliance and verify structural integrity under extreme loading, the ignition temperature was therefore manually imposed at t^* = 29.99 sec. Examination of the second propagation wave revealed that these cells experience only a moderate temperature increase of at most 39.8 K. Consequently, the ignition temperature was imposed on these six battery cells at t^* = 59.99 sec. This indicates that in this case, the EASA requirement for containment is not the critical design driver. Conversely, the requirement will become much more relevant in the event of overcharging, where all battery cells within the same parallel string experience the same voltage and may potentially enter TR simultaneously.

In this study, the cells of the third intra-module propagation wave were not assigned the heat source terms in TR in order to specifically investigate the BTMS under the EASA requirement. Nevertheless, an analysis of the temporal progression of local peak temperatures in the theoretical third propagation wave demonstrated that, under the extreme conditions of the selected initiation scenario, the hybrid cooling system cannot prevent intra-module propagation to the third propagation wave after 112 s. However, it is crucial to note that the forced ignition of the 13 cells within 60 s represents a high-energy extreme scenario selected primarily to test the EASA compliance and structural integrity of the developed BTMS.

4.2.2. Convective heat removal and thermal reserves of the coolant

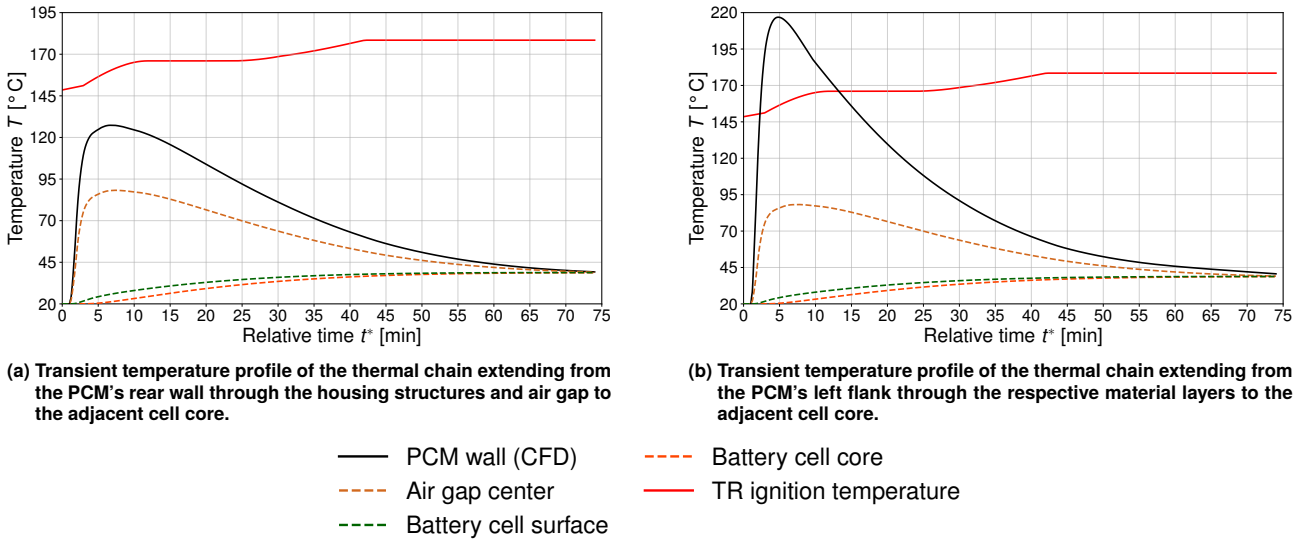
Despite the high heat input, the wall temperature of the pipe remains stable throughout the cascading process, reaching a transient peak of only 27.9 °C, while the macroscopic coolant outlet temperature rises by approximately 2.5 K to just under 22.5 °C. This high thermal stability is a direct result of the the selected mass flow rate of $\dot{m}$ = 0.1216 kg s^{-1} which yields a mean heat transfer coefficient of $h \approx$ 12 449 W m^{-2} K^{-1} for the period extending from the sudden onset of flow to the end of the phase of peak heat input (t^* = 55 s to 200 s).

However, a detailed analysis of the TR scenario reveals that thermal stability is primarily governed by the buffering effect of the PCM, whereas the thermal resistance between the cell and the coolant constitutes the limiting factor. The high heat transfer coefficient results in a high pressure drop; however, due to the limited heat flux from the module, the contribution of this pressure drop to the actual heat-sinking effect is disproportionately low. Consequently, the current design point should be viewed as a conservative upper limit; iterative optimization of the mass flow rate offers greater potential for increasing efficiency without significantly compromising the system's thermal safety. This leads to two key thermodynamic insights for the module design:

1) **Safety margin against boiling:** Since both the wall temperature and the coolant outlet temperature remain well below the critical boiling point of the coolant, the risk of local boiling is effectively mitigated due to the substantial thermal margin to the coolant's boiling point. The fluid system thus operates in a safe thermodynamically regime with wide safety margins.
2) **Potential for pressure drop optimization:** The fact that the coolant dissipates the transient thermal load without significant macroscopic overheating demonstrates that the mass flow rate was set too conservatively. Given the total pressure drop of Δp = 43.34 kPa determined in the simulation, this reveals significant optimization potential: a moderate reduction in the mass flow rate during the TR phase would disproportionately reduce pumping requirements due to the quadratic dependence of pressure drop on mass flow rate without compromising the overall system's thermal safety.

4.2.3. Analytical assessment of inter-module propagation

Since the CFD modeling terminates at the outer surface of the PCM, an explicit finite difference method was implemented to assess the risk of thermal propagation to adjacent modules. Taking into account the individual thermal resistances of the housing assembly and the thermal iner-



(a) Transient temperature profile of the thermal chain extending from the PCM's rear wall through the housing structures and air gap to the adjacent cell core.

(b) Transient temperature profile of the thermal chain extending from the PCM's left flank through the respective material layers to the adjacent cell core.

FIG 11. Transient temperature profiles obtained via the coupled transient one-dimensional multilayer post-processing analysis, evaluated against the SOC-dependent ignition temperature according to Amano et al. [23].

tia, the transient temperature profile up to the end of the mission at $t^* = 74$ min is shown for the rear of the module in Fig. 11a and the left side of the module in Fig. 11b.
The results underscore the protective effect of the hybrid cooling system. While the rear wall of the triggered battery module reaches a peak temperature of up to 127.3 °C, the 5 mm thick air gap significantly attenuates the heat input. Throughout the entire 74-minute observation period, the thermal response of the cells in the adjacent module is minimal, allowing their core temperatures to remain well below critical safety limits. Across the entire transient process, a minimum thermal safety margin of more than 128 K relative to the ignition temperature is observed. Calculations thus demonstrate that the temperature of the first row of battery cells in the adjacent module never approaches critical levels, thereby preventing thermal propagation between modules.
The physical assumption of negligible free convection within the module gap was validated by the quantitative simulation results. Based on the peak thermo-fluidic conditions, the following gap Rayleigh numbers (Ra_l) are obtained:

- Module rear: The thermal peak results in a maximum gap Rayleigh number of $Ra_{l,back} \approx 4\,282$.
- Left module flank: Similarly, a maximum value of $Ra_{l,left} \approx 5\,342$ is found for the left flank.

Since both values remain significantly below the threshold of 10^4, which is widely used as the limit for pronounced convective flow, the Nusselt number in the gap can consistently be assumed to be $Nu \approx 1$. Nevertheless, this reduction to heat conduction represents a physical abstraction. In particular, radiative heat transfer was not explicitly resolved in the present 1D model. This effect can contribute significantly to the total heat flux at wall temperatures of up to 220 °C encountered in TR. While this omission is accepted from a conservative standpoint regarding the barrier effect, it leads to an underestimation of the actual heat input into the adjacent module walls. Future model iterations should therefore incorporate radiation terms using effective emissivity values to further enhance predictive accuracy under extreme thermal loads.

4.2.4. Synthesis: EASA compliance and suitability for aviation applications

In conclusion, the suitability of the preferred hybrid cooling concept CP-light can be assessed against the EASA's restrictive aviation requirements based on the quantitative simulation results as follows:

1) **Containment of thermal propagation:** The BTMS fully meets the primary safety requirement. Although a cascading effect within the module extending to the third wave is theoretically initiated after 112.8 s under the conservative assumptions of the EASA extreme scenario (forced ignition of 13 cells within 60 s), the structural barrier effect preventing outward propagation remains intact. The analytically determined transient core and surface temperatures of battery cells in adjacent modules peak at 38.6 °C with a safety margin $>$ 126.8 K and hence remain well within the absolutely safe range. Catastrophic propagation across modules is thus physically ruled out.
2) **Lightweight design and system complexity:** With a mass fraction of the cells on the battery module of 60.56 % in the filled operating state, CP-light achieves the lightest design and saves substantial amounts of coolant compared to the CP-based design variants (19 g versus 631 g). Furthermore, the conventional bottom-side cooling plate reduces the component count to 139 individual parts (approximately half that of the CP-based design); this minimizes susceptibility to leaks and satisfies EASA requirements for a robust, low-maintenance aviation system.
3) **Thermodynamic operational reliability and safety:** During nominal operation, the system keeps the cells below the critical 35 °C threshold. While the pressure drop of 120 Pa resulting under nominal operating conditions easily meets energy efficiency requirements, the pressure drop of 43.3 kPa occurring in the TR case exceeds the idealized design target of 25 kPa.

In summary, CP-light proved successful in the numerical and subsequent analytical simulations. Nevertheless, the investigations reveal that the timing specifications of the regulatory EASA requirements only partially reflect the failure behavior of modern hybrid systems.

5. CONCLUSION

This work investigated hybrid cooling concepts for battery modules to resolve the conflict between high power density during nominal operation and passive safety in the event of thermal runaway (TR) for electric regional aviation. Based on a detailed review of the state of the art which highlighted the gap between hybrid cooling, the necessary thermal barrier effect, and the application of battery modules in electric aircraft, two hybrid designs utilizing an active cooling system (water-ethylene glycol mixture) alongside passive cooling via the phase-change material (PCM) sodium acetate trihydrate were modeled. A cooling plate (CP)-based concept was designed which combines a base-mounted cooling plate with intercellular PCM. Furthermore, a thermal conductive structure (TCS)-based design was conceived, linking intercellular TCS with a bottom layer of PCM. Both designs were investigated in a robust and in a mass-reduced version. The numerical evaluation encompassed both a transient thermal load profile for a regional passenger flight and a high-energy extreme scenario in accordance with CMT specifications.

Analysis of the simulation data revealed that all four variants reliably met the thermal requirements for nominal operation, maintaining cell temperatures below the 35°C limit. However, when considering additional aviation-specific requirements regarding low maintenance, manufacturing complexity, and weight, the mass-reduced version of the CP-based design proved to be the most suitable solution. In the event of TR, the system demonstrated its protective performance through the combination of the PCM's thermal buffer capacity and the high convective reserve of the liquid cooling system. Furthermore, as the propagation of TR between modules was successfully prevented, the mass-reduced version of the CP-based design represents a robust compromise that optimally addresses the requirements for low maintenance and gravimetric efficiency, achieving a battery cell mass fraction of over 60 %. The insights gained in this study open up various avenues for further research:

- **PCM Optimization:** Since during nominal operation the maximum battery cell temperature remained well below the minimum phase change temperature of 55 °C set during PCM selection, phase change of the PCM during nominal operation can be ruled out and the use of PCMs with lower melting temperatures such as composite PCMs could further optimize thermal buffering for TR containment. Furthermore, tailoring the thermal conductivity anisotropy in composite PCMs could accelerate the heat distribution during a TR event, thereby enhancing the efficacy of the buffer.
- **Environmental and Load Sensitivity:** In order to simulate the operation in warmer environments, extending the evaluation of the BTMS concepts to include ambient temperatures up to 45 °C and more intensive thermal load profiles due to higher discharge rates is essential to validate the system's robustness for global deployment and operation scenarios.
- **Hydraulic Optimization in TR:** Building on the pressure loss identified due to the current pipe geometry and conservatively high massflow rate, a topology-optimized channel layout should be evaluated and a sensitivity analysis focusing on reduced massflow rates should be performed to minimize pumping requirements without compromising thermal margins.
- **Realistic TR Scenarios:** The investigated TR scenario involved the forced initiation of 13 cells within a period of 60 s. This represents a rigorous test performed to satisfy the CMT's requirement for TR containment. Future studies should focus on a realistic propagation scenario through overheating, where propagation is governed by physical interaction rather than forced ignition to verify the BTMS' effectiveness under natural dynamics.
- **Variety of Failure Mechanisms:** In addition to thermal abuse, the BTMS should be evaluated against other TR triggers, such as mechanical abuse (e.g. deformation or perforation through nail penetration) or electrical abuse. Furthermore, effects such as venting and the subsequent ignition of the released gases should be addressed in subsequent studies, as these were outside the scope of the current analysis.
- **Integrative Safety Concepts:** High-performance thermal barrier materials offer significant potential to mitigate intra-module and inter-module TR propagation. Specifically, the integration of aerogel felts into the hybrid cooling architecture should be investigated as a secondary passive safety layer to prevent propagation even in the event of active cooling system failure, as they are lightweight, require no control or maintenance, and carry no risk of leakage.

References

[1] European Commission. Flightpath 2050: Europe's vision for Aviation. report of the high level group on aviation research. Report EUR 24902 EN, Publications Office of the European Union, Luxembourg, 2011.

[2] María Zamarreño Suárez, Francisco Pérez Moreno, Raquel Delgado-Aguilera Jurado, Rosa María Arnaldo Valdés, and Víctor Fernando Gómez Comendador. Battery technologies to electrify aviation: Key concepts, technologies, and figures. *International Journal of Aviation Science and Technology*, 4(2):98–112, 2023. DOI: 10.23890/IJAST.vm04is02.0205.

[3] Alperen Oğuzhan Altun, Florian Franke, and Stefan Kazula. Overview of the state of the art in battery packaging and elaboration of a safe design process for battery packs in large electric aircraft. In *Deutscher Luft- und Raumfahrtkongress 2024*, Hamburg, Germany, 2024. DocumentID: 63031. DOI: 10.25967/630310.

[4] Ahmad A. Pesaran. Battery thermal management in EV and HEV: Issues and solutions. Technical report, National Renewable Energy Laboratory (NREL), 2001.

[5] Tavish Pattanayak and Dimitri Mavris. Battery technology for sustainable aviation: a review of current trends and future prospects. *Applied Energy*, 397:126356, 2025. DOI: 10.1016/j.apenergy.2025.126356.

[6] Yongxin Lai, Weixiong Wu, Kai Chen, Shuangfeng Wang, and Chuang Xin. A compact and lightweight liquid-cooled thermal management solution for cylindrical lithium-ion power battery pack. *International Journal of Heat and Mass Transfer*, 144:118581, 2019. DOI: 10.1016/j.ijheatmasstransfer.2019.118581.

[7] Michael Murphy and Mohammad Akrami. Advanced thermal management of cylindrical lithium-

ion battery packs in electric vehicles: A comparative CFD study of vertical, horizontal, and optimised liquid cooling designs. *Batteries*, 10(8):264, 2024. DOI: 10.3390/batteries10080264.

[8] Christian Huber. *Phase Change Material in Battery Thermal Management Applications*. PhD thesis, Technische Universität München (TUM), München, 2017. https://mediatum.ub.tum.de/doc/1356376/1356376.pdf.

[9] Alperen Oğuzhan Altun, Florian Franke, and Stefan Kazula. Elaboration and evaluation of concepts for battery modules in electrified aircraft propulsion systems. In *Proceedings of the 15th EASN European Aerospace Conference*, Madrid, Spain, 2025. Presented at EASN 2025. DOI: 10.3390/engproc2026133018.

[10] Wencan Zhang, Zhicheng Liang, Xiuxing Yin, and Guozhi Ling. Avoiding thermal runaway propagation of lithium-ion battery modules by using hybrid phase change material and liquid cooling. *Applied Thermal Engineering*, 184:116380, 2021. DOI: 10.1016/j.applthermaleng.2020.116380.

[11] Wen Yang, Fei Zhou, Yuchen Liu, Shuai Xu, and Xing Chen. Thermal performance of honeycomb-like battery thermal management system with bionic liquid mini-channel and phase change materials for cylindrical lithium-ion battery. *Applied Thermal Engineering*, 188:116649, 2021. DOI: 10.1016/j.applthermaleng.2021.116649.

[12] Lihong Zhao, Guangheng Song, Xiaolin Yang, and Rongkun Pan. Experiments on the effects of liquid immersion cooling on the thermal runaway (TR) behaviors of 280 ah lithium-ion batteries subjected to different TR-triggering conditions. *Journal of Energy Storage*, 121:116358, 2025. DOI: 10.1016/j.est.2025.116358.

[13] Certification Management Team (CMT). Decision document: Thermal runaway for propulsion battery. Certification management team decision document, ANAC, EASA, FAA and TCCA, 2024. Focus on containment and propagation testing levels.

[14] Gang Wang, Chao Xu, Weiqiang Kong, Gerald Englmair, Jianhua Fan, Gaosheng Wei, and Simon Furbo. Review on sodium acetate trihydrate in flexible thermal energy storages: Properties, challenges and applications. *Journal of Energy Storage*, 40:102780, 2021. DOI: 10.1016/j.est.2021.102780.

[15] Tim Rappsilber, Nawar Yusfi, Simone Krüger, Sarah-Katharina Hahn, Tim-Patrick Fellinger, Jonas Krug von Nidda, and Rico Tschirschwitz. Meta-analysis of heat release and smoke gas emission during thermal runaway of lithium-ion batteries. *Journal of Energy Storage*, 60:106579, 2023. DOI: 10.1016/j.est.2022.106579.

[16] Reynard de Vries, Rob E. Wolleswinkel, Daniel Rosen Jacobson, Maarten Bonnema, and Sebastian Thiede. Battery performance metrics for large electric passenger aircraft. In *34th Congress of the International Council of Aeronautical Sciences*, Florence, Italy, 2024.

[17] Xuning Feng, Minggao Ouyang, Xiang Liu, Languang Lu, Yong Xia, and Xiangming He. Thermal runaway mechanism of lithium ion battery for electric vehicles: A review. *Energy Storage Materials*, 10:246–267, 2017. DOI: 10.1016/j.ensm.2017.05.013.

[18] Jeffrey Belt and Alexander Sorensen. Thermal and electrochemical analysis of thermal runaway propagation of samsung cylindrical cells in lithium-ion battery modules. *Journal of The Electrochemical Society*, 170(1):010515, 2023. DOI: 10.1149/1945-7111/aca939.

[19] John Warner. *The Handbook of Lithium-Ion Battery Pack Design: Chemistry, Components, Types, and Terminology*. Oxford, United Kingdom, 2 edition, 2024. DOI: 10.1016/B978-0-443-13807-2.00012-2.

[20] Mohanad F. Hassan, Abdul Hadi N. Khalifa, and Ahmed J. Hamad. Experimental investigation of lithium-ion battery thermal management for electric vehicles using mini channels cold plate and phase change material. *Applied Thermal Engineering*, 261:124567, 2025. DOI: 10.1016/j.applthermaleng.2025.125682.

[21] Andrey W. Golubkov, David Fuchs, Julian Wagner, Helmar Wiltsche, Christoph Stangl, Gisela Fauler, Gernot Voitic, Alexander Thaler, and Viktor Hacker. Thermal-runaway experiments on consumer Li-Ion batteries with metal-oxide and olivin-type cathodes. *RSC Adv*, 4(7):3633–3642, 2014. DOI: 10.1039/C3RA45748F.

[22] Lip Huat Saw, Yonghuang Ye, and Andrew A.O. Tay. Integration issues of lithium-ion battery into electric vehicles battery pack. *Journal of Cleaner Production*, 113:1032–1045, 2016. DOI: 10.1016/j.jclepro.2015.11.011.

[23] Kofi Owusu Ansah Amano, Elena Gimadieva, and Ulrich Krause. Comparing the thermal runaway characteristics in sodium-ion batteries and Li-Ion batteries with layered oxide cathode materials: Influence of state of charge level. *Journal of Power Sources*, 648:237414, 2025. DOI: 10.1016/j.jpowsour.2025.237414.